

FR

CERN LIBRARIES, GENEVA

50558



SCAN-9511245

TRI-PP-95-54
Aug 1995

The zero-crossing angle of the $n - p$ analyzing power

C.A. Davis^{1,2}, R. Abegg^{2,3}, A.R. Berdoz^{1,*}, J. Birchall¹, J.R. Campbell¹,
L. Gan¹, P.W. Green^{2,3}, L.G. Greeniaus^{2,3}, R. Helmer^{2,3}, E. Korkmaz^{3,†}, J. Li³,
C.A. Miller^{2,3}, A.K. Opper³, S.A. Page¹, W.D. Ramsay¹, A.M. Sekulovich¹,
V. Sum¹, W.T.H. van Oers¹, J. Zhao^{1,‡}

¹⁾ University of Manitoba, Department of Physics, Winnipeg, Manitoba, Canada
R3T 2N2

²⁾ TRIUMF, 4004 Wesbrook Mall, Vancouver, B.C., Canada, V6T 2A3

³⁾ University of Alberta, Department of Physics, Edmonton, Alberta, Canada T6G 2N5

ABSTRACT

The angles at which the $n - p$ elastic scattering neutron analyzing power, A_{00n0} , crosses zero were measured with precision at four TRIUMF energies below 300 MeV. The mean interaction energies are also measured with greater precision than in previous experiments. The results are: $E_n = 175.26 \pm 0.23$ MeV, $\theta_{zx} = 98.48^\circ \pm 0.28^\circ$; $E_n = 203.15 \pm 0.20$ MeV, $\theta_{zx} = 91.31^\circ \pm 0.18^\circ$; $E_n = 217.24 \pm 0.19$ MeV, $\theta_{zx} = 87.64^\circ \pm 0.18^\circ$; and $E_n = 261.00 \pm 0.16$ MeV, $\theta_{zx} = 80.18^\circ \pm 0.19^\circ$. After correction for charge symmetry breaking effects, the energy where the *averaged* neutron-proton analyzing power crosses zero at $\theta_{zx} = 90^\circ$ is found to be $E_n = 206.8 \pm 0.6$ MeV.

(Submitted to Physical Review C)

* Presently at: Dept. of Physics, Carnegie-Mellon University, 5000 Forbes Ave., Pittsburgh, PA, U.S.A. 15213

† Presently at: Physics Department, University of Northern British Columbia, 3333 University Way, Prince George, BC, Canada V2N 4Z9

‡ Presently at: Laboratory for Nuclear Science, MIT, 77 Massachusetts Ave., Cambridge, MA 02139, USA

I. INTRODUCTION

A full understanding of the nucleon-nucleon interaction is essential both to the construction of modern potentials [1] [2] and the use of either these potentials or the phenomenologically-determined phase shifts [3] [4] [5] [6] in the construction of nuclear models. Although the data base for these phase shift fits is now quite extensive, it cannot be concluded that the phase shifts are complete and well established [7]. At TRIUMF a number of higher-precision $n - p$ experiments have been carried out with this in mind [8] [9] [10] [11]. The present experiment reported here measures the angle at which the neutron analyzing power in $n - p$ elastic scattering, A_{00n0} , crosses zero at four energies below 300 MeV.

Below 300 MeV the zero-crossing angle of the analyzing power, θ_{zx} , is strongly dependent on the incident neutron energy. This is also true of the slope of the analyzing power as a function of angle at θ_{zx} , $\left. \frac{dA_n}{d\theta} \right|_{zx}$. The scattering matrix may formally be written as [12]

$$M_I(\mathbf{k}_f, \mathbf{k}_i) = \frac{1}{2} \{ (a_I + b_I) + (a_I - b_I)(\sigma_1 \cdot \mathbf{n})(\sigma_2 \cdot \mathbf{n}) + (c_I + d_I)(\sigma_1 \cdot \mathbf{m})(\sigma_2 \cdot \mathbf{m}) \\ + (c_I - d_I)(\sigma_1 \cdot \mathbf{l})(\sigma_2 \cdot \mathbf{l}) + e_I(\sigma_1 + \sigma_2) \cdot \mathbf{n} \} \quad (1)$$

where the scattering amplitudes a_I , b_I , c_I , d_I and e_I are complex functions of the energy and scattering angle; the subscript I refers to either the isotriplet ($I = 1$) or isosinglet ($I = 0$) state, and \mathbf{l} , \mathbf{m} , and \mathbf{n} are the basis vectors of an orthogonal right-handed coordinate system defined in terms of the directions of the initial and final momenta (\mathbf{k}_i and \mathbf{k}_f) of the incident and scattered particle (neutron) as follows:

$$\mathbf{l} = \frac{\mathbf{k}_f + \mathbf{k}_i}{|\mathbf{k}_f + \mathbf{k}_i|}, \quad \mathbf{m} = \frac{\mathbf{k}_f - \mathbf{k}_i}{|\mathbf{k}_f - \mathbf{k}_i|}, \quad \mathbf{n} = \frac{\mathbf{k}_i \times \mathbf{k}_f}{|\mathbf{k}_i \times \mathbf{k}_f|} \quad (2)$$

Only M_1 applies in the $p - p$ or $n - n$ systems; both M_0 and M_1 are relevant in the $n - p$ system. A full description of M_0 requires that both the real and imaginary parts of the five scattering amplitudes be determined. Since, in determining any scattering matrix, an overall phase may be ignored (for the NN system), one is left with bilinear relationships between nine unknowns; though below the inelastic threshold this reduces to five because of unitarity [13]

The analyzing power is written in terms of these scattering amplitudes as

$$\sigma A_{00n0} = \sigma A_n = Re\{a^* e\}, \quad (3)$$

where it is understood that the amplitudes a and e include both the $I = 0$ and $I = 1$ components. The latter is usually presumed to be fixed by $p - p$ data when treating $n - p$ scattering. Note that the five complex amplitudes are a consequence of the spin $\frac{1}{2} - \frac{1}{2}$ interaction and the validity of charge, time

reversal and parity symmetries. Charge Symmetry Breaking (CSB) introduces an additional amplitude in the $n - p$ system and then $A_{00n0} \neq A_{000n}$, where the position of the non-zero subscript indicates an n -oriented polarization for the incident (neutron) or target (proton) particle respectively. Thus, at θ_{zx} , and ignoring CSB, at each energy:

$$\text{Re}\{a^* e\} = 0 \quad (4)$$

Following the nomenclature of Arndt *et al.* [4], one can write these amplitudes as

$$a = \frac{z}{k} \sum_j \{(2j+1)T_{jj}G_j + D_{j-}F_j + 2s^2D_{j0}G_j + D_{j+}P_j\} \quad (5)$$

and

$$e = -i\frac{s}{k} \sum_j \{(2j+1)T_{jj}G_j + D_{j-}F_j + 2(s^2 - \frac{1}{z})D_{j0}G_j + D_{j+}P_j\}, \quad (6)$$

where k is the center-of-mass momentum, $z = \cos\theta$, and $s = \sin\theta$, θ being the center-of-mass scattering angle.

$$G_j = \frac{P_j^1}{j(j+1)}, \quad (7)$$

$$F_j = P_j - G_j z, \quad (8)$$

where the $P_j(z)$ are Legendre polynomials and $P_j^1(z)$ are associated Legendre functions of order 1, also

$$D_{j-} = (j+1)T_{j-} + jT_{j+} - 2\sqrt{j(j+1)}T_{j0}, \quad (9)$$

$$D_{j0} = j(j+1)\{T_{j-} - T_{j+}\} + \sqrt{j(j+1)}T_{j0}, \quad (10)$$

$$D_{j+} = jT_{j-} + (j+1)T_{j+} + 2\sqrt{j(j+1)}T_{j0}, \quad (11)$$

where the T_{jj} are the triplet uncoupled partial-wave amplitudes (e.g., 3D_2), and T_{j-} , T_{j0} and T_{j+} are the triplet coupled partial-wave amplitudes (e.g., 3S_1 , ϵ_1 and 3D_1 , respectively). Note that the analyzing power does not contain any singlet partial-wave amplitudes (other than through the normalization by the cross section), so they do not influence θ_{zx} . Also, except for the $\frac{1}{z}$ term in the e amplitude, all of the cross terms defined in the product of a and e vanish at $z = 0$ (i.e., 90°). For $I = 1$, this term, proportional to G_j , is zero for even- j since $P_j^1(z = 0) = 0$; whereas, for $I = 0$, the odd- j P_j^1 do not vanish. This is consistent with the $p - p$ analyzing power being constrained to vanish at 90° due to the symmetry of identical particles. For the $n - p$ analyzing power this non-vanishing $I = 0$ term is responsible for moving the zero-crossing away from 90° .

Equation (4), when fully expanded, gives a long but conceptually simple expansion in terms of the differences of the phase shifts, *viz.*, $\sin 2(\delta_A - \delta_B)$ where

A and B are any two partial waves mentioned above. Thus the *change* in θ_{zx} as a function of energy is most sensitive to the triplet partial-waves that vary significantly over the energy range observed here. Figure 1 shows the triplet partial-wave phases that change by at least 3° over the energy range from 160 to 480 MeV [14] (the largest change is more than 30°). From this we can see that 3S_1 , 3D_1 (for $I = 0$), 3P_0 , and 3P_1 (for $I = 1$) change by better than 10° and should have the greatest impact on A_n .

II. EXPERIMENTAL METHOD

The experiment was realized at the TRIUMF neutron beam facility (beamline 4A/2) [15] [16]. The layout of the experiment and neutron production facility is presented in Figure 2. The detector systems and other equipment used were developed for two charge symmetry experiments that measured the difference in θ_{zx} for beam polarized - target unpolarized (A_{oono}) and beam unpolarized - target polarized (A_{oono}) conditions [17] [18] [19]. This section contains a brief summary describing the essential elements of this facility and detector systems, though there is more detailed explanation of calibration procedures and measurements unique to this experiment.

A. Primary proton beam

The production of a polarized proton beam at TRIUMF makes use of the $d(\vec{p}, \vec{n})pp$ reaction, using a sideways-to-sideways spin transfer, τ_t , which is large in magnitude. The primary polarized proton beam extracted from the TRIUMF cyclotron into beamline 4A passes through two polarimeters. The first polarimeter [20] is a large-acceptance four-branch polarimeter measuring both normal and sideways transverse components of polarization. It is located 7.21 m upstream of the center of the liquid deuterium neutron-production target (LD_2). Each branch has two in-line scintillators in the forward arm (at 17°) with conjugate backward-arm scintillators to observe the coincidences with the recoil protons. $p - p$ scattering from a thin ($\sim 200 \frac{\mu\text{g}}{\text{cm}^2}$) Para-xylylene-N [21] target was used to monitor the proton beam polarization. The second polarimeter [22] is a two-branch low-acceptance ($\sim 6\%$ of the first polarimeter's acceptance) polarimeter that measures only the normal polarization. It is of similar construction with 17° forward arms and conjugate recoil counters using $p - p$ scattering from a $0.0003''$ ($\sim 1 \frac{\text{mg}}{\text{cm}^2}$) Kapton [23] foil. Valid $p - p$ scattering events requiring a forward and appropriate recoil arm coincidence were counted in sets of beam spin-state (up, down, off) gated scalers, as were *accidentals*, i.e., coincidences with a 43 ns delay, corresponding to the cyclotron RF period, to correct for random coincidences. Separate calibrations with thin graphite foils replacing the para-xylylene-N or Kapton targets were used to correct the results for contributions from ${}^{12}\text{C}(p, pp)X$ reactions. Cross-checks were also made against CH_2 foils in each polarimeter. The accidental and carbon quasi-elastic corrected values were used to calculate the proton polarization.

Immediately behind both branches of the second polarimeter are two Beam Energy Monitors (BEMs) consisting of six-scintillator range counter stacks preceded by a series of copper degrader pieces. The scattered protons passing through the forward arms of the polarimeter range out in these stacks, the signals of which are formed into the following sequence of logic pulses

$$N_j = Pol \cdot \prod_i^j R_i, \quad j = 1, 2, 3, 4, 5, 6, \quad (12)$$

where Pol refers to a valid $p-p$ scattering proton from the polarimeter and R_i to a signal in the i^{th} scintillator in the range counter stack. The thickness of copper degrader is chosen so that the protons from free $p-p$ scattering range-out in the stack. This thickness must, of course, be adjusted at each energy. The logic pulses are counted in a set of scalers which also counts the corresponding *accidental* signals from the polarimeter. The difference between these scaled logic signals

$$\Delta_j = N_{j+1} - N_j, \quad j = 1, 2, 3, 4, 5, \quad (13)$$

constitutes a distribution of stopping protons. The $p-p$ peak observed in this distribution is a measure of the energy of the scattered protons, and, therefore, the energy of the proton beam. By measuring the apparent beam energy from both the left and right branches of the second polarimeter, the average energy can be determined and is found to be independent of small displacements of the beam from the polarimeter center line. A resolution of 35 keV in the *relative* energy is achievable in a few minutes [15]. A measurement was done of the efficiency of each of the scintillators in the BEM's relative to the first scintillator in the stack (which is smaller than the others and thus defines the BEM acceptance) by raising the energy to 497 MeV and looking at protons that pass through to the rearmost scintillator. For both BEMs and in all cases the middle four scintillators had measured efficiencies of $\geq 99.9\%$ (note that the last scintillator, though its absolute efficiency is not measured, does not stop any valid $p-p$ scattered events under normal circumstances). As the passing protons used in the above mentioned efficiency calibration were depositing only $\sim \frac{1}{5}$ the energy in each scintillator as a stopping proton would, it is safe to assume that there is no efficiency skew of the BEM range peak.

As θ_{zx} is a strong function of energy, it is necessary to have an accurate measurement of the *absolute* energy of the neutron beam. This requires an accurate measurement of the absolute energy of the primary proton beam and accurate knowledge of the neutron beam energy profile. To accomplish the former it was necessary to calibrate the BEMs. This was done by taking advantage of another experiment which measured the $np \rightarrow d\pi^0$ cross section near threshold [24]. This experiment was done on TRIUMF's CHARGEX [25] facility on the 4B beamline using the 0° neutrons produced from the ${}^7\text{Li}(p,n){}^7\text{Be}$ reaction. Deuterons, produced in the $np \rightarrow d\pi^0$ reaction by the neutrons impinging on a liquid hydrogen target, were detected in the Medium Resolution Spectrometer (MRS). The locus of deuteron momentum vs. angle is a strong function of the neutron energy, especially close to pion threshold. At one of their lower energies, $E_n = 276.98$

MeV (less than 2 MeV above the pion threshold), the beam was transferred to beamline 4A (by simply turning off the dipole that had been deflecting it down 4B) and thus through the second proton polarimeter target which scatters into the BEMs. No adjustments were made to any parameters in the actual cyclotron tune which might affect the extracted energy. This allows the establishment of calibrated range distributions in the BEMs at that energy. At the lowest energy of Ref. [24], for which the deuteron locus fell entirely into the acceptance of the MRS, it was possible to establish an error on their neutron energy of ± 30 keV, and to compare this, by using the peak from elastically scattered recoil protons, to their other energies whose uncertainties are consequently dominated by this ± 30 keV. The proton beam energy is unfolded from the neutron energy and from energy losses in the ${}^7\text{Li}$ target. This procedure takes into account that the neutron yield from the first excited state at 0.43 MeV in ${}^7\text{Be}$ was calculated [24] to be 83% of the ground state yield. This was done by combining the spectroscopic factors measured by Austin *et al.* [26] with the value $|\frac{d_{px}}{d_r}|^2 = 11$ taken from Alford *et al.* [27]. Neutrons from higher unbound states of ${}^7\text{Be}$ were of no consequence since in all cases they have energies below the threshold for pion production.

This established a calibration for a single (highest) energy in the present experiment. To calibrate the three remaining energies the proton beam was scattered off a thin CH_2 target and the scattered protons observed in the MRS centered at 15° . The position of the peak of elastically scattered protons from ${}^{12}\text{C}$ was measured and the MRS dipole field recorded for each of the four energies. At each energy the beam was switched between beamlines 4A and 4B without adjustment to the cyclotron parameters and, therefore, proton beam energy. The BEM's were thus calibrated to beam energies which took into account energy losses in the MRS target, windows and detectors, and the momentum dispersion corrections to slight position errors for the proton peaks (this latter was cross-checked against the position of the first inelastic peak from ${}^{12}\text{C}$). The carbon elastic peak was preferred to the $p-p$ peak as the kinematics shift very little over the acceptance of the MRS in the former case. Thus, the calibration of all four energies is linked directly to that of the highest energy whose calibration is established by the well-understood kinematics of the $np \rightarrow d\pi^0$ reaction.

B. Neutron beam

The proton beam impinges on the 21.7 cm long LD_2 target encased in a shielded housing with a stepped iron collimator centered at 9° to beam left. Immediately downstream of the LD_2 target the proton beam is deflected 35° to the right, passes through a beam clean-up collimator, and is directed toward the 4A beam dump which is separately shielded in another part of the experimental hall. The neutrons scattered at 9° pass through the collimator into the 4A/2 neutron experimental area. Just upstream of the LD_2 target is a solenoid which precesses the proton spin from vertical to sideways orientation. The sideways-to-sideways spin transfer parameter, R_t , for free $n-p$ scattering at 9° (lab.) is

known to be large and negative at all TRIUMF energies. The polarized neutrons have their spins precessed into the longitudinal direction by a vertical field dipole (they are already partially precessed by their passage through a corner of the 35° bender that deflects the proton beam to the beam dump), and then into a normal (vertical) direction by a horizontal field dipole. In addition to the main transverse neutron polarization component, for a perfectly sideways transversely polarized proton beam, there will be a very small sideways to longitudinal spin transfer, R'_t , and, polarized or not, there will be a small inherent normal polarization of the neutron beam created in the $d(p, n)pp$ reaction. The latter component ends up as a longitudinal component of the neutron polarization at the experimental target. The true picture is a bit more complicated, as we do not have a target of free neutrons. The corrections to obtain the quasifree spin transfer parameters (r_t and r'_t) for $d(\vec{p}, \vec{n})pp$ were calculated, along with the neutron energy spectrum, by Bugg and Wilkin [28]. The energy dependence of the neutron spectrum and r_t and r'_t , plus energy loss in the LD_2 target, and the collimator geometry, were all included in a Monte Carlo modelling of the TRIUMF neutron area that has been described in Ref. [16]. The solenoid and two neutron spin-precession dipoles were calibrated to maximize the spin transfer, i.e., $\sqrt{r_t^2 + r'_t^2}$, and thus the neutron polarization, using neutron polarimeters located before the first neutron spin-precession dipole and after the experimental apparatus. However, it should be noted that the consequences of having small non-normal components of the neutron beam are negligible as, in a single spin-analyzing power measurement, they can have no effect on the in-plane asymmetries due to parity conservation.

The two neutron polarimeters were each four-branch devices capable of measuring both transverse polarization components of the neutron beam. With the two spin-precession dipoles in between, they effectively measured all three components of neutron polarization, with the over all calibration coming from the beam-averaged value of spin transfer and the measurement of the proton polarization. The neutron polarimeter data were read into a set of spin-state gated scalars.

The position of the neutron beam was monitored, at an error of about ± 1 mm, by a profile monitor located immediately upstream of the second neutron polarimeter. This consisted of a veto scintillator followed by a conversion scintillator and two delay line wire chambers (DLC's) spaced apart far enough to allow reconstruction of charged particle tracks back to the conversion scintillator and, thus, to provide a profile of the neutron beam at that point, 3.65 m downstream of the experimental target. The profile monitor data were read as a separate event into the data stream with a pre-scaler to adjust the fraction of profile monitor events to a reasonable level.

C. Experimental target

The target for this experiment was a $2 \times 3.5 \times 5 \text{ cm}^3$ (32.13 g) CH_2 block mounted on a pin and kept balanced by thin copper strips. A similar block of clean graphite (26.24 g, compared to 27.54 g of carbon in the CH_2 target) was

used for background measurements. The 5 cm length was oriented vertically for both targets. The targets were oriented to minimize the amount of material through which the lower energy protons (at the rear angle acceptance of the proton detectors) had to pass, thereby minimizing their multiple scattering. At the lowest energy, the “booms” of the proton detector systems were both centered at just over 40°, the targets were oriented with the thinner dimension parallel to the beamline. For the other three energies, at which the booms were at progressively more backward angles, the thin dimension of the targets was placed perpendicular to the beam.

D. Recoil proton detection system

The recoil protons were detected in two detector assemblies mounted on “booms” symmetrically placed around the neutron beam. Each boom supported a time-of-flight (TOF) system for energy determination and a set of four DLC's for track reconstruction, grouped in pairs fore and aft, and was positionable to within 0.02°. The booms were raised or lowered through a hydrostatic system which allowed for precision height adjustment and leveling.

The proton TOF system consisted of a 1.6 mm thick start scintillator viewed by photo-multiplier tubes (PMTs) top and bottom and two 6.4 mm thick stop scintillators each viewed by four PMTs. The TOF start counters were 290 mm from target center, and the two stop counters were 1715 and 1870 mm from target center. The timing information from the stop counters was calibrated as a function of proton hit position and a weighting factor for each tube determined from the inverse square of the width of each timing peak at that position. At some positions, i.e., near the corners of the counters, only three tubes were used, as the light collection of the fourth tube was inefficient in these cases. The two independent measurements of the proton TOF stops were used to determine an averaged proton energy.

The DLC's each had an active area of $58 \times 58 \text{ cm}^2$. All chambers consisted of single anode planes sandwiched between cathode foils. The spacing between the planes was kept constant by flowing the chamber gas under pressure in such a way as to counterbalance the electrostatic attraction between the cathode and anode planes. The signals on the cathode planes (one running horizontally, the other vertically) were capacitively coupled to delay lines and timing signals were read out at both ends. The differences between the timing signals provided a position coordinate (either x or y) to ≤ 1 mm. Each DLC was aligned on the boom to a precision of 0.5 mm. External pulser signals coupled to known positions on the delay lines monitored any timing drifts so that the relative alignment of the DLC's could be maintained throughout the duration of the experiment to a precision of about ± 0.2 mm.

E. Scattered neutron detection system

Scattered neutrons were detected in two large identical scintillator arrays placed at angles corresponding to the elastic recoil angle setting of the proton booms. Each array consisted of two stacked banks of seven 1.05 m long \times 0.15 m deep \times 0.15 m high scintillator bars, one bank behind the other. Each bar was viewed by two PMTs, one at each end. The time difference between the PMT signals provided an x position coordinate for the neutron. The y position was determined from knowledge of which bar or bars were hit. The x position resolution for charged particles was ~ 2 cm and it is estimated that the resolution is a little worse for neutrons; the y resolution is taken as ± 7.5 cm, half a bar thickness. The neutron arrays to target distances and the horizontal transverse positions were determined with an accuracy of 2 mm. The arrays were positioned vertically and levelled to an accuracy of ≤ 1 mm. The time sum from the neutron bar PMT's, combined with a corrected start signal from the proton TOF start counter, determined the neutron TOF and, thus, energy. To discriminate against charged particles, three overlapping scintillator panels were placed in front of each array.

F. Data collection procedure

The timing and pulse height information was latched into CAMAC TDC's and ADC's. The existence of valid proton and valid neutron triggers within a reasonable time resolution was taken as an indication of an $n-p$ event. In this case, the data was read from the TDC's and ADC's along with information from a coincidence register that recorded information on the spin state of the beam. The spin orientation was changed from "up" to "down" after an interval of one minute in each state, with 15 second spin "off" periods interspersed. The latter served as a check for the instrumental asymmetries of the polarimeters. As mentioned above, the neutron profile monitor data were recorded as a separate event class. A pulser system to the detectors artificially generated the main $n-p$ event trigger in a random manner. These "pulser" events allowed for later dead-time corrections (important for background subtraction) and provided some detector calibrations and stability monitoring. Flags for the pulser events, along with signals identifying "left" and "right" detector systems, as defined by the physical direction of scattering of the neutron, were also recorded in the coincidence register. Scaler information, including that for the polarimeters and BEM's, was read separately at five second intervals. All of this information was buffered and then written to tape via a J-11 Starburst [29] processor and a VAX 3100 [30] computer. The latter supported an on-line analysis software package that allowed us to sample and monitor the data as it was collected.

III. ANALYSIS

The data analysis involved: (i) selection of the $n-p$ elastic scattering events based on cuts on a number of kinematical parameters; (ii) determination of

the angle of scattering (based on the proton) for each event and formation of histograms of the angular distributions for left/right events and up/down spin states; (iii) study of the background data and subtraction from the CH_2 target data; (iv) calculation of scattering asymmetries and extraction of θ_{zx} and the slope at θ_{zx} ; (v) analysis of the BEM information to compare the data run energies to the calibrations; (vi) analysis of the polarimeter information to determine the primary proton polarization; and (vii) analysis of various monitor information, such as the neutron beam profile events, to establish various corrections and estimate systematic errors.

A. Selection of neutron-proton elastic events

For $n-p$ elastic scattering, assuming the incident neutron energy to be known, only two kinematic variables need be known, usually chosen as the polar and azimuthal angles of one of the particles, one to determine the kinematics, the other to specify the orientation. In fact, the following parameters were determined in the analysis: θ_n , ϕ_n , θ_p , ϕ_p , E_{scat} , and Δp_x (horizontal momentum balance) - the latter two arise from determination of proton and neutron TOF - so that each event was four times kinematically overdetermined. Given that two angles are effectively used (the data are binned according to θ_{cm}), the cuts were placed on the opening angle ($\theta_n + \theta_p$ less the kinematically expected value at the central angle), coplanarity ($\phi_n + \phi_p - 180^\circ$) and horizontal momentum balance. In addition, there was an effective measurement of the incident neutron energy, E_{inc} , from the measurement of the recoil proton TOF start (corrected for the flight-time from the target) compared to the cyclotron RF signal. The latter had been stabilized during the run and read into a TDC for each event. Corrections were made to it for long term drifts (basically a motion of the proton bunches within the phase acceptance of the cyclotron). It effectively measures the TOF of the neutron from the LD_2 production target to the experimental target. This provided two additional parameters: the energy difference, $\Delta E_n = E_{inc} - E_{scat}$ and the average of the two (almost) independent energy measurements, $E_n := \frac{1}{2}(E_{inc} + E_{scat})$, upon which cuts were placed. Histograms of the following variables: opening angle, coplanarity, ΔE_n , and E_n are presented in Figure 3. In all cases, all other cuts are present on the displayed variable. This figure also shows the background measurement results scaled for integrated beam, target mass, and live-time.

The skew of the opening angle peak (Fig. 3a) arises from differences in multiple scattering as a function of proton energy correlated with θ_p . As out-scattered events will not be recorded by the proton detector system, but in-scattered events will be, the average measured θ_p at the large θ_p edge will be smaller (where E_p is smallest and the multiple scattering is larger). Thus the peak is enhanced on the shoulder below the expected angle ($< 0^\circ$ in Fig. 3a). The graphite background measurement is mismatched at the shoulders as the correlation between proton energy and θ_p no longer holds and the multiple scattering is different without significant free hydrogen in the target. In fact there is a small hint of some free hydrogen in the graphite target in the small bump at 0° .

The coplanarity (Fig. 3b) is broader than the opening angle because the error

in the measurement of ϕ_n is large, determined from whichever neutron bar was hit (± 7.5 cm). Cuts on both opening angle and coplanarity eliminate significant amounts of $C(n, np)$ background and double-scattered neutrons or protons as well.

The energy difference, ΔE_n (Fig. 3c), has a lower energy tail arising from multiple scattering of recoil protons lengthening the path length and, therefore, proton TOF. High and low ΔE_n tails can arise from tails in the time structure of the primary proton beam. The timing of the bunch may move around inside the full phase acceptance of the cyclotron of $\sim 35^\circ$ (4 ns) [31] which also explains the long term drift of the RF mentioned above.

A histogram for the neutron beam spectrum is illustrated in Fig. 3d. The spread arises from the intrinsic kinematics of the $d(p, n)pp$ reaction, energy losses in the LD_2 target, the geometry of the neutron beam collimation, the acceptance and resolution of the detector systems (E_{scat}), and the resolution and stability of the RF determination of the incident neutron's TOF (E_{inc}) [16]. The low energy tail arises from the $d(p, n)pp$ kinematics, and is gradually cut off as the recoil proton energy ranges out in the detector system without triggering the proton TOF stop.

Cuts were placed on each of these parameters and the horizontal momentum balance. These cuts were varied in the range of 2.5 to 3.5 times the σ for the variable. The neutron beam energy (Fig. 3d), however, is a unique case as it actually has a finite distribution as explained above. The low energy cut thus dictates what neutrons are being selected in the data base and, therefore, what the average neutron energy will be. These cuts are presented in Table 1. This will be considered below in greater detail in the Beam Energy sub-section, III.C. The cuts on coplanarity, ΔE_n , and horizontal momentum balance were varied and had no noticeable effect on the θ_{zx} results, but the cuts on the opening angle could, as this parameter was most susceptible to be skewed by multiple scattering effects. This will be discussed below in the systematic errors section.

The DLC information was also used to reconstruct the target vertex and cuts were made to ensure that events were coming from the target. Tracking information was also used to calculate flight paths for both the neutron and proton and, in the latter case, were corrected for very small deflections in the fringe field of the cyclotron.

Approximately 37% to 41% (the fraction drops with increasing beam energy) of all events were useful $n - p$ events. The carbon background determined from the graphite target runs was $\sim 0.2\%$ to 0.3% , see Table 1. The events were binned by neutron center-of-mass angle based on the proton angle information derived from the DLC's. Spectra were made for left/right events and up/down spin states. The same was done for the graphite target data which, after rescaling for integrated beam flux, target mass (carbon) difference, and live time, were subtracted from the CH_2 target data.

B. Asymmetry calculation

The scattering asymmetry for a particular angular bin may be extracted from

$$\epsilon = \frac{r - 1}{r + 1}, \quad (14)$$

where

$$r = \sqrt{\frac{L^+ R^-}{R^+ L^-}}, \quad (15)$$

and where L and R refer to left and right events and $+$ and $-$ refer to up and down spin. Calculating the asymmetry with this procedure cancels all systematic errors not correlated with beam polarization reversals to at least first order [18]. The analyzing powers thus extracted are displayed for all four energies in Figure 4. The data sets may be found in full in Table 2. Each of these data sets has been fit to the following relationship:

$$A_n = \frac{dA_n}{d\theta} \{(\theta - \theta_{zx}) + c(\theta - \theta_{zx})^2 + d(\theta - \theta_{zx})^3\}, \quad (16)$$

where θ_{zx} , as previously explained, is the zero-crossing angle, $\frac{dA_n}{d\theta}$ is the slope at θ_{zx} , and c and d are higher order curvature parameters fixed at values determined from [14]. The error on θ_{zx} determined from this fit depends on the slope, $\frac{dA_n}{d\theta}$, as well as the counting errors on the data presented in Fig. 4.

C. Beam energy calculation

The proton beam energy calibration procedure explained at the end of section II.A. resulted in four \times two calibrated stopping distributions in each of the BEMs. These were compared to the distributions collected during the actual experiment run-time and the four primary proton beam energies were calculated. These are presented in Table 3 along with the error estimates.

The neutron beam energies were calculated from the known E_p values and the measured densities in the LD_2 target as input to the Monte Carlo simulation mentioned in section II.B [16]. These Monte Carlo simulations had to be compared to the measured E_n . To do this they were convoluted with the detector acceptance, the $n - p$ cross-section, and a detector response function that had a Gaussian distribution in the TOF domain whose σ was approximated by the σ determined from the ΔE_n parameter. The latter was in effect an upper bound, as the E_{scat} TOF start and E_{inc} TOF stop were dependent on the same counter. The resolution of the proton TOF start counter was measured to be 0.26 ns (both tubes averaged together). This is small compared to the averaged proton TOF stop counter resolution, uncertainties in the recoil proton and scattered neutron flight path, or to the phase width of the primary proton bunches versus RF. Best fit σ 's of this convoluted detector response function compared to

$\frac{1}{2}\sigma_{\Delta E_n}$'s were consistently $\sqrt{(\frac{1}{2}\sigma_{\Delta E_n})^2 - (\sigma_{fit})^2} \simeq 0.2-0.3$ ns smaller, see Table 1. These convoluted predictions plus experimental errors were compared to the data [16] and found to explain the shape of the E_n well, but usually with a small under-estimation of the data in the low energy side of the peak. They were used to calibrate the data energy scale and, thus, the lower cut-off energies for E_n , see Table 1. The predictions also included the values for spin transfer parameters, r_t and r'_t as a function of neutron energy. The neutron polarization is, therefore, given by

$$P_n(E_n) = P_p \times \sqrt{r_t^2(E_n) + r'_t{}^2(E_n)} \times f(E_n), \quad (17)$$

where $f(E_n)$ takes into account the variation in spin precession as a function of neutron energy through the magnets (this is actually rather negligible as the neutron energy distributions are relatively narrow compared to their peak energies).

As explained at the end of the last section, the error on θ_{zx} is related to the asymmetry slope. Thus

$$\delta\theta_{zx} \propto \frac{1}{P(E_n)\frac{dA_n}{d\theta}(E_n)}, \quad (18)$$

where $\frac{dA_n}{d\theta}(E_n)$ is the slope of the analyzing power at θ_{zx} . Therefore, the average energy determined across a spectrum of neutrons, $\sigma(E_n)$, is given by

$$\langle E \rangle = \frac{\int_{E_l} [P(E_n)\frac{dA_n}{d\theta}(E_n)]^2 \sigma(E_n) E_n dE_n}{\int_{E_l} [P(E_n)\frac{dA_n}{d\theta}(E_n)]^2 \sigma(E_n) dE_n}, \quad (19)$$

where E_l is the cut given in Table 1. The energy dependence of the polarization is determined from the Monte Carlo [16] as explained above. The energy dependence of the analyzing power slope, $\frac{dA_n}{d\theta}$, is determined from the data. The results for the weighted average neutron energy are given in Table 3; these values and errors being calculated to a precision of ~ 30 keV. Ignoring the energy dependence of $P(E_n)$ and $\frac{dA_n}{d\theta}(E_n)$ would result in a systematic error of about 1 MeV.

D. Polarization calculation

The proton polarization, is given in Table 4 for each energy. The values have been corrected for accidentals and $C(p,pp)$ background and used polarimeter analyzing powers based on Ref. [14] which are integrated across the polarimeter acceptance. The average neutron polarization is determined by an integration over the values of r_t and r'_t derived from the Monte Carlo simulation [16]

$$\langle P_n \rangle = \frac{\int_{E_l} P(E_n)\sigma(E_n)dE_n}{\int_{E_l} \sigma(E_n)dE_n} = P_p \frac{\int_{E_l} \sqrt{r_t^2(E_n) + r'_t{}^2(E_n)}\sigma(E_n)dE_n}{\int_{E_l} \sigma(E_n)dE_n}. \quad (20)$$

These are also given in Table 4.

However, additional structure below the peak of the incident neutron spectrum that is unexplained by the Monte Carlo simulation [16] (the under-estimation mentioned above in section III.C) must also be considered. The fraction of this within the cuts is reported in Table 4. This is believed [16] to arise principally from neutrons rescattered in the LD_2 target and nearby shielding and, as this occurs over many angles and initial energies, is taken to have zero polarization within a ± 0.2 error. Thus, this has no effect for the energy averaging reported in III.C. However, the average polarization is reduced by a few per cent. This effect has been included in the results presented in Tables 3 and 4.

E. Neutron beam position

As mentioned in Section II.B, a neutron profile monitor constantly monitored the position of the neutron beam. The beam was found to be consistently ~ 8 mm displaced horizontally (~ 0.6 mr) at the proton monitor target, in agreement with a known LD_2 target misalignment [16]. This was stable to within ± 1 mm. Due to the mirror symmetry of the detection apparatus, the data-averaging cancels this effect on the determination of θ_{zx} .

F. Systematic errors

As mentioned in Section II.D, the positioning error of the booms was $\pm 0.02^\circ$ in the laboratory reference frame. The positioning error of ± 0.5 mm in each DLC on the booms, over an average separation of 0.9 m between the two groups of DLC's, corresponds to an angle error of $\pm 0.03^\circ$ in the lab. The uncertainty in the location of the pulser fiducials was ± 0.7 mm over the same average separation, which contributes an error of $\pm 0.04^\circ$ in the lab. The differential non-linearity of the TDC's, the DLC binning error, and the error of the neutron beam position apply only to individual events and average out over the whole acceptance and left-right symmetry of the apparatus. The background was directly subtracted from the data, as mentioned at the end of Section III.A and its error is reflected in the statistical error that is quoted for the final results. In terms of the center-of-mass angle, the total angle error is $\pm 0.11^\circ$ from all effects combined quadratically.

The errors in the neutron beam energy were presented in Table 3. The product of this error and the slope of θ_{zx} with respect to the energy gives the angle error due to the uncertainty in the energy. The errors in the zero crossing angles, based on slopes deduced from the data, are also presented in Table 3.

The normalization error arises from the errors on the polarization of the neutron beam. This depends on the statistical error in determining the proton polarization (including $C(p,pp)$ calibrations), the ± 0.005 error in the geometrically-averaged $p-p$ analyzing power as estimated from variations in the phase shift solutions given in Ref. [14], and the errors deduced for the polarization averaging as discussed in Section III.D. These are presented as the errors on P_n in Table 4 and as the relative errors to the normalization scale in the captions of Table 2. These errors are used to generate the systematic errors for the slope, $\frac{dA_n}{d\theta}$,

quoted in Table 5.

IV. RESULTS

The results for θ_{zx} are presented in Table 5. There is a strong energy dependence of θ_{zx} which is seen in Figure 5a, which also includes data from IUCF [32] and from previous TRIUMF measurements [11]. The data are compared to the prediction from Ref. [14]. To emphasize the deviations of this data from present phase shift analysis (PSA) predictions, Figure 5b presents the deviation of the data from the PSA predictions. Both the IUCF and previous TRIUMF measurements report an uncertainty in beam energy of ± 2 MeV. The corresponding uncertainty in θ_{zx} as a function of energy is represented by the two solid lines in Fig. 5b. The significantly lower errors reported for our absolute beam energy measurements mean that the present experiment has measured $\theta_{zx}(E)$ to the highest accuracy yet achieved. As we measure only the neutron polarized analyzing power, there is in principle a correction due to charge symmetry breaking, between that and the average analyzing power, which is presented [33] in Table 5. From this data we determine that $\theta_{zx} = 90^\circ$ at $E_n = 206.8 \pm 0.6$ MeV. The slope as a function of energy is also presented in Table 5 and in Figure 6.

V. CONCLUSION

Fig. 5b clearly indicates that the present data indicate a slightly smaller curvature for θ_{zx} than is presently predicted from Ref. [14]. The slope, $\frac{dA}{d\theta}(E_n)$, is also in slight disagreement, dropping somewhat faster to the minimum than predicted, as shown in Fig. 6. The energy at which $\theta_{zx} = 90^\circ$ varies over a range of 20 MeV for several recent PSA solutions [14], though the most recent fit (SP94) gives 205.9 MeV, only one and a half σ away from the value of 206.8 ± 0.6 MeV reported here.

Because there are several phases that are important it is not possible to draw conclusions regarding a single phase from just this one experiment. Inclusion of the present data in the PSA data base will better constrain the fit.

ACKNOWLEDGMENTS

We wish to thank TRIUMF Operations Staff for their efforts and support and D. C. Healey for assistance operating and information on the LD_2 neutron-production target. We also wish to thank R. Roper and P. Gormley of the TRIUMF Machine Shop. Thanks also to J. Martin and D. Reitzner for measurements of the time resolution of the proton TOF counters. This work was supported by a grant from NSERC (Canada).

VI. REFERENCES

- [1] M. Lacombe, B. Loiseau, J.M. Richard, R. Vinh Mau, J. Côté, P. Pirès and R. de Tourreil, Phys. Rev. C **21**, 861 (1980); W.N. Cottingham, M. Lacombe, B. Loiseau, J.M. Richard and R. Vinh Mau, Phys. Rev. D **8**, 800 (1973); R. Vinh Mau, in *Mesons in Nuclei*, edited by M. Rho and D. Wilkinson (North-Holland, Amsterdam, 1979); M. Lacombe, B. Loiseau, R. Vinh Mau, J. Côté, P. Pirès and R. de Tourreil, Institut de Physique Nucléaire (Orsay) Report No. IPNO/TH 80-60 (1980), and references therein (unpublished).
- [2] R. Machleidt, K. Holinde and Ch. Elster, Phys. Rep. **149**, 1 (1987); K. Holinde and R. Machleidt, *ibid.* **A256**, 479 (1976); K. Kotthof, K. Holinde, R. Machleidt and D. Schütte, *ibid.* **A242**, 429 (1975); X. Bagnoud, K. Holinde and R. Machleidt, Phys. Rev. C **29**, 1792 (1984); M.M. Nagels, T.A. Rijken and J.D. de Swart, Phys. Rev. D **20**, 1633 (1979); and references therein.
- [3] R.A. Arndt, R.H. Hackman and L.D. Roper, Phys. Rev. C **9**, 555 (1974); *ibid.* **15**, 1002 (1977); *ibid.* **15**, 1021 (1977).
- [4] R.A. Arndt, L.D. Roper, R.A. Bryan, R.B. Clark, B.J. ver West and P. Signell, Phys. Rev. D **28**, 97 (1983).
- [5] D.V. Bugg *et al.*, J. Phys. G **4**, 1025 (1978); D.V. Bugg *et al.*, Phys. Rev. C **21**, 1004 (1980).
- [6] J. Bystricky, C. Lechanoine-Leluc and F. Lehar, J. Phys. (Paris) **48**, 199 (1987).
- [7] D.V. Bugg, Comments Nucl. Part. Phys. **12**, 287 (1984).
- [8] C.A. Davis, in *High Energy Spin Physics: Eighth International Symposium*, edited by K. Heller (AIP, No. **187**, New York, 1989), 572, vol. 1.
- [9] R. Abegg *et al.*, Phys. Rev. C **38**, 2173 (1988).
- [10] D. Bandyopadhyay *et al.*, Phys. Rev. C **40**, 2684 (1989).
- [11] R. Abegg *et al.*, Phys. Rev. C **40**, 2406 (1989).
- [12] P. LaFrance and P. Wintermütz, J. Phys. **41**, 1391 (1980); J. Bystricky *et al.*, J. Phys. **39**, 1 (1978).
- [13] L. Puzikov *et al.*, Soviet Physics - JETP **5(32)**, 489 (1957).
- [14] R.A. Arndt, I.I. Strakovsky and R.L. Workman, Phys. Rev. C **50**, 2731 (1994); and Interactive Dial-in Program SAID, SP94 solution.
- [15] R. Abegg *et al.*, Nucl. Instr. and Meth. **A234**, 11 (1985).
- [16] L. Gan *et al.*, Nucl. Instr. and Meth. A (in press).
- [17] R. Abegg *et al.*, Nucl. Instr. and Meth. **234**, 20 (1985).
- [18] R. Abegg *et al.*, Phys. Rev. D **39**, 2464 (1989); R. Abegg *et al.*, Phys. Rev. Lett. **56**, 2571 (1986).

- [19] R. Abegg *et al.*, Nucl. Instr. and Meth. **B79**, 318 (1993).
- [20] R. Abegg and R. Schubank, TRIUMF Report No. TRI-DN-87-17, 1987 (unpublished).
- [21] Para-xylylene-N obtained from Parmat Inc., 958 Bassett Rd., Cleveland, Ohio 44145, U.S.A.
- [22] L.G. Greeniaus and J. Soukup, TRIUMF Report No. TRI-DN- 81-1, 1981 (unpublished).
- [23] Kapton, a polyimide foil obtained from Dupont.
- [24] D.A. Hutcheon *et al.*, Nucl. Phys. **A535**, 618 (1991); D.A. Hutcheon *et al.*, Phys. Rev. Lett. **64**, 176 (1990).
- [25] R. Helmer, Can. J. Phys. **65**, 588 (1987).
- [26] S.M. Austin, L.E. Young, R.R. Doering, R. DeVito, R.K. Bhowmik and S.D. Schery, Phys. Rev. Lett. **44**, 972 (1980).
- [27] W.P. Alford *et al.*, Phys. Lett. **179**, 20 (1986).
- [28] D.V. Bugg and C. Wilkin, Nucl. Phys. **A467**, 575 (1987).
- [29] J-11 Starburst ACC2180 fast front-end processor from CES of Petit Lancy, Switzerland.
- [30] VAX 3100 from Digital Equipment Corp. of Maynard, Mass., U.S.A.
- [31] W.D. Ramsay, N.E. Davison, D.A. Hutcheon, R. Laxdal and J. Pearson, Nucl. Instr. and Meth. **A237**, 265 (1993).
- [32] J. Sowinski *et al.*, IUCF Sci. and Tech. Report 1989-1990, 9 (1990).
- [33] M.J. Iqbal (private communication).

List of Tables

Table 1. Low energy limits on the neutron beam energy and corresponding fractions of $C(n, np)$ background.

Table 2. Analyzing power and errors as a function of neutron center-of-mass angle for the four energies. The common normalization error due to the uncertainty in the neutron beam polarization is given for each energy.

Table 3. The weighted average neutron energies corresponding to the low energy limits on the neutron distributions as listed in Table 1 and the corresponding incident proton energies. The error on the zero-crossing angle due to the uncertainty in the neutron beam energy is given in the third column.

Table 4. The $p - p$ analyzing powers (A_p) at 17° in the laboratory from Ref. [14], the average measured proton beam polarization, the average spin transfer determined from Ref. [16], and the deduced average neutron polarization which

includes a correction and error from the fraction of unexplained structure (in the Monte Carlo modelling) given in the last column.

Table 5. Measured zero-crossing angles and slopes of the $n - p$ analyzing power at θ_{zx} for the given energies. The first error is statistical, the second error is the systematic error.

List of Figures

Figure 1. The nucleon-nucleon triplet partial-wave phases that change by at least 3° over the energy range, as obtained from the SP94 solution in Ref. [14].

Figure 2. The layout of the experiment and neutron production facility (TRIUMF beamline 4A/1 & 4A/2). The proton beam passes through two polarimeters (the second contains the Beam Energy Monitor) and a spin precession solenoid before impinging on the LD_2 target and then being bent by the clearing magnet to the beam dump. The resultant neutrons, with predominantly sideways polarization, pass through a collimator and two spin precession dipoles, which places the neutron polarization in the vertical direction as the neutrons arrive at the target location. The neutrons scatter into the neutron arrays and the recoil protons pass through the scintillators and DLC's arranged on booms at the conjugate angle. The neutron beam also passes through two polarimeters and a profile monitor.

Figure 3. Histograms of some relevant kinematic variables for data obtained at 203.15 MeV incident neutron energy: (a) opening angle, (b) coplanarity, (c) ΔE_n , and (d) raw E_n . The CH_2 target (solid symbols) measurement and the graphite target background (open symbols) measurement (results scaled for integrated beam, target mass, and live time) are presented with a logarithmic ordinate (counts). Each variable reflects cuts on all other variables.

Figure 4. The extracted analyzing powers for the four energies: (a) 175.26 MeV, (b) 203.15 MeV, (c) 217.24 MeV, and (d) 261.00 MeV. The curves are the fits to equation (16).

Figure 5. (a) The measured values of θ_{zx} determined in the present experiment (solid squares), the IUCF results (open circles) [32], and previous TRIUMF results (open triangles) [11] are compared to the SP94 predictions from Ref. [14]. To emphasize the differences of this data from the predictions, they are presented in (b) with the PSA estimates subtracted. Both the IUCF and previous TRIUMF measurements estimate errors in beam energy of ± 2 MeV. That cor-

responding error on θ_{zx} as a function of energy is represented by the two solid lines in (b). The present data include their smaller energy error (see Table 3) added in quadrature to the total error bars.

Figure 6. The slope, $\frac{dA_n}{d\theta}$ at θ_{zx} as a function of neutron energy. The present data (solid squares) and the data from Ref. [11] (open circles) are compared to the predictions from Ref. [14] (SP94).

Table 1.

E_n (MeV)	Energy cut (MeV)	Background %	$\sqrt{(\sigma_{\Delta E_n})^2 - (\sigma_{fit})^2}$ (ns)
175.26	155.60	0.27	0.3
203.15	180.26	0.30	0.3
217.24	192.25	0.27	0.2
261.00	232.90	0.18	0.2

Table 2.

$E_n = 175.26 \pm 0.23$ MeV Scale Error = 4.9%		
θ_n (degrees, c.m.)	Analyzing Power	Error
86.13	0.0928	0.0176
86.38	0.1225	0.0173
86.63	0.1232	0.0175
86.88	0.1413	0.0173
87.13	0.0859	0.0174
87.38	0.1136	0.0173
87.63	0.1223	0.0171
87.88	0.0981	0.0171
88.13	0.0985	0.0171
88.38	0.1122	0.0171
88.63	0.0874	0.0173
88.88	0.0917	0.0172
89.13	0.0890	0.0171
89.38	0.0723	0.0171
89.63	0.0846	0.0170
89.88	0.0676	0.0170
90.13	0.0572	0.0172
90.38	0.0782	0.0171
90.63	0.1009	0.0170
90.88	0.0513	0.0169
91.13	0.0984	0.0166
91.38	0.0674	0.0170
91.63	0.0819	0.0168
91.88	0.0561	0.0169
92.13	0.0555	0.0168
92.38	0.0716	0.0168
92.63	0.0236	0.0167
92.88	0.0573	0.0167
93.13	0.0248	0.0167
93.38	0.0250	0.0167
93.63	0.0644	0.0166
93.88	0.0240	0.0166
94.13	0.0542	0.0165
94.38	0.0481	0.0167
94.63	0.0460	0.0165
94.88	0.0491	0.0165
95.13	0.0390	0.0166
95.38	0.0161	0.0164
95.63	0.0035	0.0165

$E_n = 175.26 \pm 0.23 \text{ MeV}$ Scale Error = 4.9%		
θ_n (degrees, c.m.)	Analyzing Power	Error
95.88	0.0402	0.0165
96.13	0.0338	0.0165
96.38	0.0311	0.0164
96.63	0.0090	0.0164
96.88	-0.0024	0.0163
97.13	0.0037	0.0163
97.38	-0.0169	0.0163
97.63	0.0163	0.0164
97.88	0.0306	0.0163
98.13	-0.0072	0.0163
98.38	-0.0208	0.0162
98.63	0.0117	0.0163
98.88	-0.0203	0.0162
99.13	-0.0076	0.0162
99.38	-0.0247	0.0162
99.63	-0.0052	0.0161
99.88	0.0146	0.0162
100.13	0.0114	0.0161
100.38	0.0022	0.0161
100.63	-0.0114	0.0162
100.88	-0.0259	0.0161
101.13	-0.0011	0.0161
101.38	-0.0146	0.0162
101.63	-0.0215	0.0162
101.88	-0.0325	0.0163
102.13	0.0169	0.0165
102.38	-0.0472	0.0164
102.63	-0.0406	0.0165
102.88	0.0079	0.0166
103.13	-0.0596	0.0165
103.38	-0.0418	0.0164
103.63	-0.0568	0.0165
103.88	-0.0540	0.0166
104.13	-0.0596	0.0167
104.38	-0.0506	0.0169
104.63	-0.0584	0.0169
104.88	-0.0145	0.0170
105.13	-0.0321	0.0171
105.38	-0.0691	0.0174

$E_n = 175.26 \pm 0.23 \text{ MeV}$ Scale Error = 4.9%		
θ_n (degrees, c.m.)	Analyzing Power	Error
105.63	-0.0384	0.0176
105.88	-0.0545	0.0178
106.13	-0.0279	0.0179
106.38	-0.0325	0.0183
106.63	-0.0376	0.0185
106.88	-0.0568	0.0185

$E_n = 203.15 \pm 0.20$ MeV Scale Error = 4.7%		
θ_n (degrees, c.m.)	Analyzing Power	Error
77.13	0.2034	0.0181
77.38	0.1913	0.0177
77.63	0.1930	0.0177
77.88	0.2001	0.0171
78.13	0.1703	0.0170
78.38	0.1845	0.0170
78.63	0.1651	0.0167
78.88	0.1637	0.0168
79.13	0.1865	0.0167
79.38	0.1570	0.0168
79.63	0.1364	0.0167
79.88	0.1368	0.0167
80.13	0.1726	0.0165
80.38	0.1752	0.0166
80.63	0.1164	0.0166
80.88	0.1267	0.0168
81.13	0.1184	0.0165
81.38	0.1184	0.0166
81.63	0.0995	0.0166
81.88	0.1101	0.0166
82.13	0.1582	0.0165
82.38	0.1223	0.0168
82.63	0.1000	0.0165
82.88	0.1104	0.0166
83.13	0.0950	0.0166
83.38	0.0736	0.0167
83.63	0.0684	0.0166
83.88	0.0999	0.0165
84.13	0.0924	0.0167
84.38	0.1137	0.0164
84.63	0.0830	0.0166
84.88	0.0858	0.0163
85.13	0.0885	0.0165
85.38	0.0752	0.0164
85.63	0.0960	0.0164
85.88	0.0832	0.0165
86.13	0.0665	0.0165
86.38	0.0783	0.0163
86.63	0.0768	0.0165

$E_n = 203.15 \pm 0.20$ MeV Scale Error = 4.7%		
θ_n (degrees, c.m.)	Analyzing Power	Error
86.88	0.0524	0.0167
87.13	0.0276	0.0165
87.38	0.0268	0.0164
87.63	0.0537	0.0164
87.88	0.0211	0.0165
88.13	0.0389	0.0164
88.38	0.0257	0.0164
88.63	0.0442	0.0164
88.88	0.0387	0.0165
89.13	0.0301	0.0165
89.38	0.0402	0.0165
89.63	0.0078	0.0166
89.88	0.0102	0.0164
90.13	0.0153	0.0164
90.38	0.0414	0.0164
90.63	0.0105	0.0165
90.88	0.0144	0.0165
91.13	0.0128	0.0165
91.38	-0.0216	0.0165
91.63	-0.0249	0.0165
91.88	-0.0173	0.0165
92.13	0.0188	0.0165
92.38	-0.0199	0.0164
92.63	-0.0067	0.0165
92.88	-0.0348	0.0165
93.13	-0.0181	0.0165
93.38	-0.0175	0.0165
93.63	-0.0305	0.0165
93.88	-0.0257	0.0160
94.13	-0.0244	0.0165
94.38	-0.0518	0.0165
94.63	-0.0103	0.0165
94.88	-0.0223	0.0165
95.13	-0.0388	0.0165
95.38	-0.0547	0.0165
95.63	-0.0339	0.0165
95.88	-0.0309	0.0165
96.13	-0.0352	0.0165
96.38	-0.0524	0.0160

$E_n = 203.15 \pm 0.20$ MeV Scale Error = 4.7%		
θ_n (degrees, c.m.)	Analyzing Power	Error
96.63	-0.0463	0.0160
96.88	-0.0356	0.0161
97.13	-0.0791	0.0160
97.38	-0.0430	0.0159
97.63	-0.0498	0.0158
97.88	-0.0310	0.0159
98.13	-0.0810	0.0159
98.38	-0.0900	0.0161
98.63	-0.0640	0.0158
98.88	-0.0590	0.0158
99.13	-0.0700	0.0157
99.38	-0.0645	0.0158
99.63	-0.0515	0.0160
99.88	-0.0680	0.0160
100.13	-0.0828	0.0158
100.38	-0.0821	0.0159
100.63	-0.0948	0.0158
100.88	-0.0696	0.0160
101.13	-0.0788	0.0160
101.38	-0.0834	0.0162
101.63	-0.0866	0.0163
101.88	-0.0985	0.0162

$E_n = 217.24 \pm 0.19$ MeV Scale Error = 4.5%		
θ_n (degrees, c.m.)	Analyzing Power	Error
77.13	0.1753	0.0201
77.38	0.1403	0.0202
77.63	0.1196	0.0199
77.88	0.1398	0.0196
78.13	0.1208	0.0193
78.38	0.1099	0.0192
78.63	0.0865	0.0191
78.88	0.0952	0.0192
79.13	0.1144	0.0189
79.38	0.1439	0.0187
79.63	0.0938	0.0188
79.88	0.1284	0.0186
80.13	0.0926	0.0185
80.38	0.1059	0.0188
80.63	0.0581	0.0187
80.88	0.0781	0.0186
81.13	0.0674	0.0189
81.38	0.0863	0.0186
81.63	0.0832	0.0187
81.88	0.1021	0.0186
82.13	0.0832	0.0187
82.38	0.0768	0.0188
82.63	0.0647	0.0186
82.88	0.0795	0.0186
83.13	0.0739	0.0187
83.38	0.0699	0.0188
83.63	0.0375	0.0188
83.88	0.0171	0.0188
84.13	0.0508	0.0186
84.38	0.0745	0.0185
84.63	0.0214	0.0187
84.88	0.0211	0.0188
85.13	0.0451	0.0190
85.38	0.0215	0.0186
85.63	0.0437	0.0186
85.88	0.0188	0.0186
86.13	0.0268	0.0186
86.38	0.0019	0.0187

$E_n = 217.24 \pm 0.19$ MeV Scale Error = 4.5%		
θ_n (degrees, c.m.)	Analyzing Power	Error
86.63	0.0193	0.0190
86.88	0.0123	0.0189
87.13	0.0164	0.0185
87.38	-0.0102	0.0186
87.63	0.0151	0.0186
87.88	-0.0037	0.0186
88.13	-0.0037	0.0187
88.38	-0.0301	0.0188
88.63	-0.0020	0.0184
88.88	-0.0273	0.0186
89.13	-0.0246	0.0186
89.38	0.0013	0.0187
89.63	-0.0236	0.0188
89.88	-0.0419	0.0187
90.13	-0.0406	0.0186
90.38	-0.0196	0.0185
90.63	-0.0020	0.0184
90.88	-0.0241	0.0186
91.13	-0.0077	0.0184
91.38	-0.0575	0.0186
91.63	-0.0565	0.0182
91.88	-0.0497	0.0183
92.13	-0.0392	0.0183
92.38	-0.0378	0.0185
92.63	-0.0115	0.0185
92.88	-0.0331	0.0185
93.13	-0.0566	0.0185
93.38	-0.0527	0.0184
93.63	-0.0739	0.0183
93.88	-0.0693	0.0183
94.13	-0.0759	0.0185
94.38	-0.0285	0.0185
94.63	-0.0458	0.0184
94.88	-0.0705	0.0184
95.13	-0.0789	0.0182
95.38	-0.0702	0.0183
95.63	-0.0847	0.0184
95.88	-0.0519	0.0184

$E_n = 217.24 \pm 0.19$ MeV Scale Error = 4.5%		
θ_n (degrees, c.m.)	Analyzing Power	Error
96.13	-0.0887	0.0181
96.38	-0.0867	0.0182
96.63	-0.0693	0.0182
96.88	-0.0898	0.0182
97.13	-0.1018	0.0181
97.38	-0.1092	0.0184
97.63	-0.0973	0.0181
97.88	-0.0926	0.0181
98.13	-0.0792	0.0182
98.38	-0.0949	0.0181
98.63	-0.1204	0.0180
98.88	-0.1074	0.0181
99.13	-0.0833	0.0181
99.38	-0.0711	0.0180
99.63	-0.1231	0.0179
99.88	-0.0912	0.0180
100.13	-0.0934	0.0181
100.38	-0.0958	0.0182
100.63	-0.1096	0.0180
100.88	-0.1010	0.0180
101.13	-0.1237	0.0182
101.38	-0.1260	0.0183
101.63	-0.1224	0.0185
101.88	-0.1280	0.0187

$E_n = 261.00 \pm 0.16 \text{ MeV}$ Scale Error = 4.1%		
θ_n (degrees, c.m.)	Analyzing Power	Error
68.13	0.2353	0.0239
68.38	0.2137	0.0238
68.63	0.1818	0.0241
68.88	0.1861	0.0241
69.13	0.1686	0.0242
69.38	0.1552	0.0243
69.63	0.1623	0.0240
69.88	0.1709	0.0242
70.13	0.2152	0.0242
70.38	0.1705	0.0246
70.63	0.1775	0.0244
70.88	0.1394	0.0251
71.13	0.1694	0.0250
71.38	0.1025	0.0252
71.63	0.1721	0.0252
71.88	0.1684	0.0253
72.13	0.1657	0.0255
72.38	0.1108	0.0258
72.63	0.1311	0.0258
72.88	0.0858	0.0260
73.13	0.1066	0.0259
73.38	0.0870	0.0262
73.63	0.1268	0.0260
73.88	0.1555	0.0261
74.13	0.1020	0.0262
74.38	0.0955	0.0262
74.63	0.1253	0.0260
74.88	0.0796	0.0259
75.13	0.0582	0.0259
75.38	0.0603	0.0259
75.63	0.0582	0.0258
75.88	0.0463	0.0258
76.13	0.0862	0.0259
76.38	0.0611	0.0258
76.63	0.0807	0.0253
76.88	0.0266	0.0260
77.13	0.0534	0.0256
77.38	0.0818	0.0257

$E_n = 261.00 \pm 0.16 \text{ MeV}$ Scale Error = 4.1%		
θ_n (degrees, c.m.)	Analyzing Power	Error
77.63	0.0153	0.0255
77.88	0.0761	0.0255
78.13	0.0237	0.0250
78.38	0.0533	0.0252
78.63	0.0015	0.0253
78.88	-0.0101	0.0248
79.13	0.0429	0.0250
79.38	-0.0082	0.0247
79.63	0.0087	0.0247
79.88	-0.0189	0.0248
80.13	-0.0279	0.0243
80.38	-0.0096	0.0242
80.63	-0.0253	0.0244
80.88	0.0326	0.0243
81.13	-0.0255	0.0244
81.38	-0.0567	0.0239
81.63	-0.0379	0.0240
81.88	-0.0310	0.0242
82.13	-0.0353	0.0243
82.38	-0.0163	0.0242
82.63	0.0061	0.0242
82.88	-0.0256	0.0240
83.13	-0.0739	0.0240
83.38	-0.0473	0.0240
83.63	-0.0324	0.0239
83.88	-0.0380	0.0241
84.13	-0.0763	0.0241
84.38	-0.0913	0.0241
84.63	-0.0832	0.0240
84.88	-0.0743	0.0241
85.13	-0.0353	0.0242
85.38	-0.0866	0.0241
85.63	-0.0234	0.0239
85.88	-0.0757	0.0238
86.13	-0.0710	0.0240
86.38	-0.1035	0.0241
86.63	-0.1000	0.0241
86.88	-0.0977	0.0241

$E_n = 261.00 \pm 0.16$ MeV Scale Error = 4.1%		
θ_n (degrees, c.m.)	Analyzing Power	Error
87.13	-0.0948	0.0242
87.38	-0.0969	0.0240
87.63	-0.1217	0.0243
87.88	-0.0995	0.0241
88.13	-0.1267	0.0243
88.38	-0.1182	0.0243
88.63	-0.0880	0.0239
88.88	-0.1221	0.0241
89.13	-0.0808	0.0241
89.38	-0.1010	0.0242
89.63	-0.1360	0.0245
89.88	-0.0907	0.0245

Table 3.

E_n (MeV)	E_p (MeV)	$\delta\theta_{zx}$
175.26 ± 0.23	192.15 ± 0.10	$\pm 0.07^\circ$
203.15 ± 0.20	220.60 ± 0.10	$\pm 0.05^\circ$
217.24 ± 0.19	235.01 ± 0.09	$\pm 0.04^\circ$
261.00 ± 0.16	279.77 ± 0.07	$\pm 0.02^\circ$

Table 4.

E_n #	A_p	P_p %	Average Spin Transfer	P_n %	Unexplained Structure (%)
175.26	0.2810	68.8 ± 0.9	-0.822 ± 0.015	56.5 ± 2.8	2.3
203.15	0.3215	72.4 ± 0.8	-0.838 ± 0.017	59.6 ± 2.8	4.5
217.24	0.3399	70.3 ± 0.9	-0.855 ± 0.015	59.4 ± 2.7	3.0
261.00	0.3875	68.2 ± 0.7	-0.834 ± 0.017	56.6 ± 2.3	5.1

Table 5.

E_n (MeV)	θ_{zx} (degrees)	ΔCSB (degrees)	$\frac{dA_n}{d\theta}$ (degrees) ⁻¹
175.26	$98.48 \pm 0.28 \pm 0.11$	-0.19	$-0.00754 \pm 0.00033 \pm 0.00037$
220.60	$91.31 \pm 0.18 \pm 0.11$	-0.20	$-0.01074 \pm 0.00025 \pm 0.00050$
217.24	$87.64 \pm 0.18 \pm 0.11$	-0.21	$-0.01164 \pm 0.00029 \pm 0.00053$
261.00	$80.18 \pm 0.19 \pm 0.11$	-0.17	$-0.01549 \pm 0.00043 \pm 0.00063$

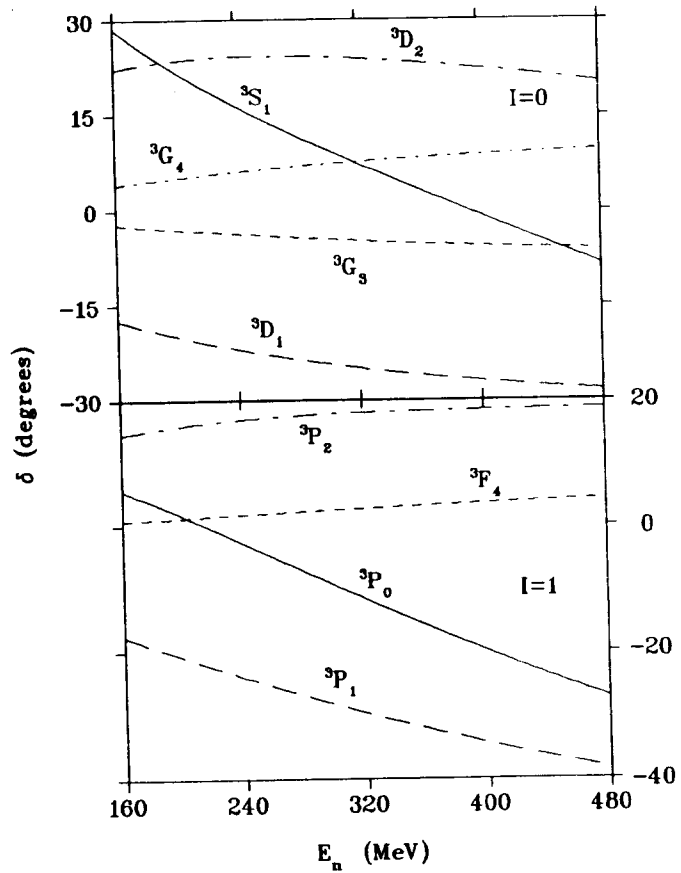


Fig. 1

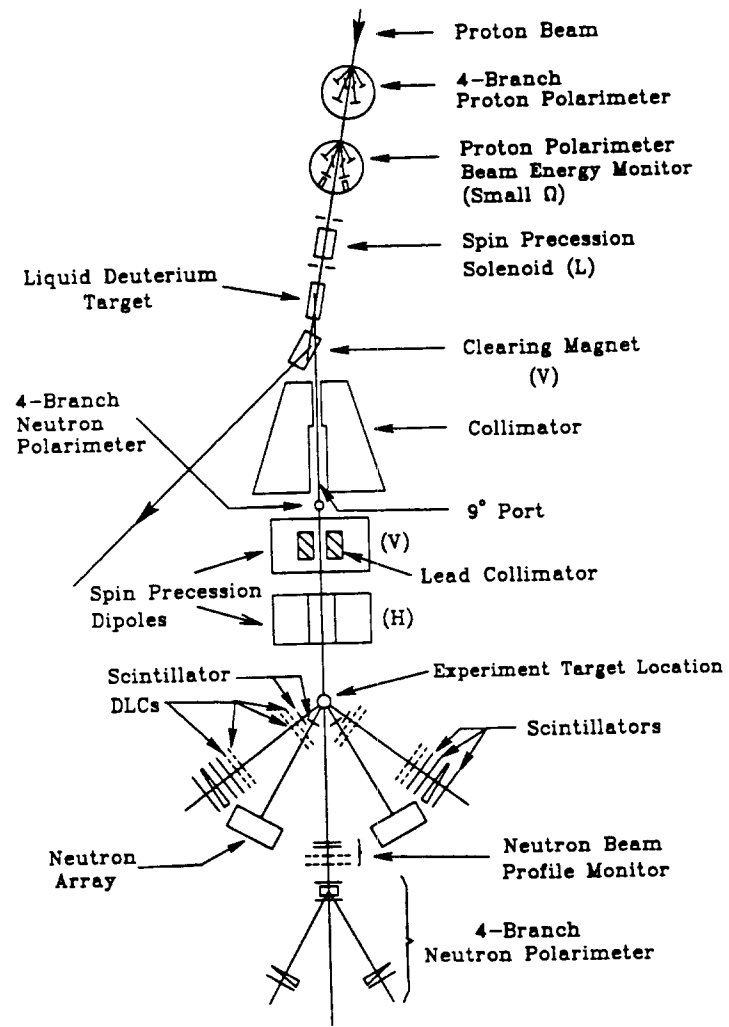


Fig. 2

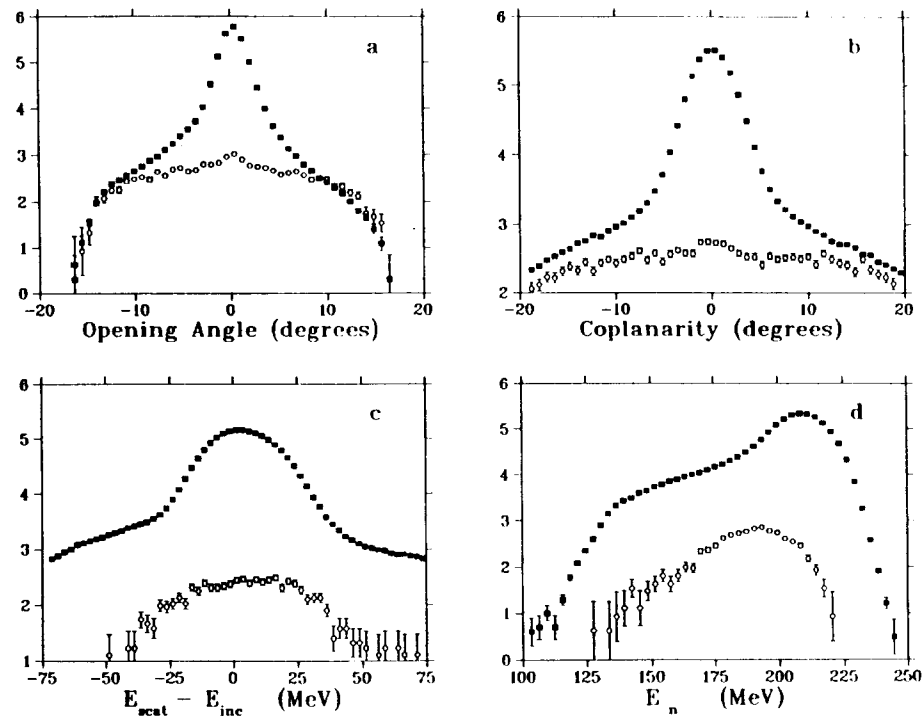


Fig. 3

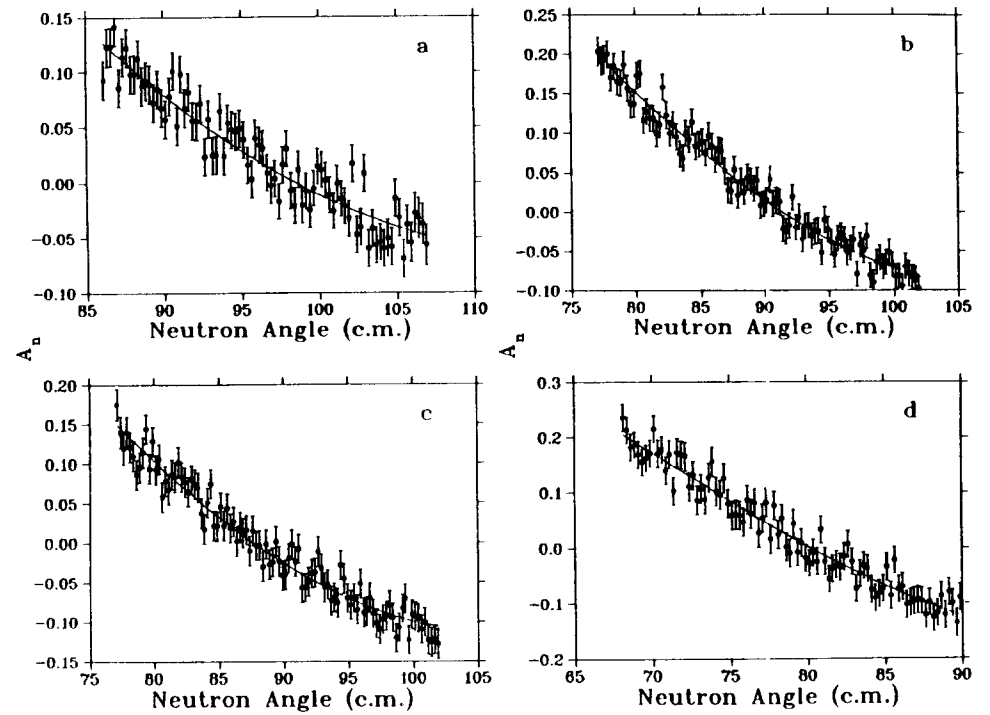


Fig. 4

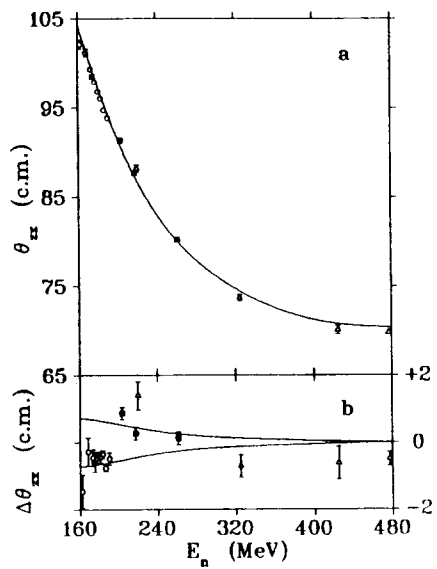


Fig. 5

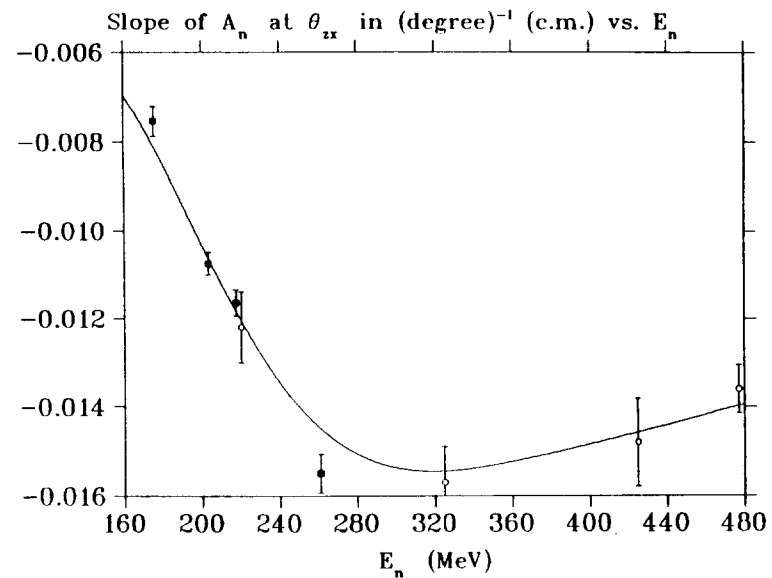


Fig. 6